Optics Letters

Space–time focusing in a highly multimode fiber via optical pulse shaping

Bohao Liu* and Andrew M. Weiner

School of Electrical and Computer Engineering, Purdue University, West Lafayette, Indiana 47907, USA
**Corresponding author: liubohao@purdue.edu*

Received 25 June 2018; revised 23 August 2018; accepted 24 August 2018; posted 28 August 2018 (Doc. ID 335796); published 21 September 2018

Fields propagating through a highly scattering material will be distorted in both space (intensity speckles) and time (spectral and temporal speckles), inhibiting tasks such as imaging and communication in both the optical and radio frequency regions. In optics, research thus far has demonstrated spatial focusing, image transmission, and short pulse delivery through bulk scattering materials and multimode fibers by taking advantage of spatial wavefront-shaping techniques. Here, we exploit spectral phase shaping for reference-free characterization of spectral and temporal speckle, and space–time focusing of broadband ultrafast pulses distorted by modal dispersion in a multimode fiber. We show that temporal speckle fields at different multimode fiber output locations are uncorrelated and demonstrate the ability to focus a short pulse at a specific output spatial location, while keeping the field at other output locations noise-like, offering opportunities to expand multimode fiber imaging and communication capacity.

https://doi.org/10.1364/OL.43.004675

A highly scattering environment scrambles a propagating field in both space and time, making tasks such as imaging and communication problematic in a wide range of areas. Scattering of waves has been extensively studied in radio frequency (RF) wireless transmission [1–3] and acoustics [4–6], for which direct time domain measurements are possible. In optics, direct measurements of the field are ruled out due to the much higher frequencies. However, it is well known that strong distortion of the optical wavefront results in a noise-like field, with intensity speckle patterns in space in the case of a single-frequency input light [7]. Taking advantage of spatial light modulator technologies, wavefront shaping [8–13] has been applied to overcome spatial distortions in strongly scattering bulk materials, thereby achieving spatial control of the diffusive light. For the case of broadband input light, speckle also arises in time and frequency; different random substructures in the time and frequency dimensions are seen at each specific output location [13,14]. The intensity correlation of speckle patterns with frequency has been studied for characterization of the scattering impulse response [15,16]. Experiments in [17–20] demonstrated spatiotemporal focusing of ultrafast pulses through a bulk scattering medium via wavefront-shaping techniques. Such experiments open up possibilities for enhancing two-photon nonlinear processes and improving microscopy in turbid samples.

Propagation through multimode fibers (MMFs) can also lead to speckle-like phenomena in space, frequency, and time. Here, the distortions arise from the superposition of different guided modes and modal dispersion. Aside from their traditional use for short-distance communication links, MMFs have received significant recent research attention for coherent image transmission [21,22], mode-division multiplexing for high-speed optical communications [23,24], quantum research [25], and multimode complex nonlinear optics [26,27]. Overcoming and utilizing speckle-like distortions caused by modal dispersion scattering in MMFs is of interest for such applications. Inspired by wavefront-shaping experiments in bulk scattering materials, spatial focusing through MMF has been achieved using wavefront shaping controlled by different methods such as transmission matrix measurements [25,28] and optical phase conjugation [29]. This has led to a potential for medical-use endoscopes with improved resolution and compactness, and with all-optical (versus mechanical) scanning control. In connection with broadband light, correlation techniques have been used to study the frequency dependence of intensity speckle patterns at the output of MMFs, and to realize a MMF-based spectrometer [30,31]. Techniques for characterizing the time domain output of MMFs illuminated by ultrashort pulse input were reported in Refs. [32,33]. In Refs. [34,35], ultrashort pulses were delivered through MMF via a wavefront-shaping technique, in which short pulses transmitted through and distorted by the MMF interfere with an ultrashort reference pulse to form a time-gated digital hologram containing spatial phase information. The short pulses were delivered by the spatially shaped reference counterpropagating through the same MMF with spatial mode-selective phase conjugation process. Such work has promise for nonlinear optical imaging through fiber and may have relevance for optical communications in MMF.

Here, for the first time to our knowledge, we perform reference-free characterization of spectral and temporal speckles at different spatial positions on the output face of a MMF, and achieve space–time focusing involving all the excited propagating modes (note that portions of this work were previously presented at a conference [36]). Transform-limited

pulses are formed locally at the MMF output by compensating the spectral phase response via optical pulse shaping [37,38]. The concept is analogous to our group's work on temporal shaping of ultrawideband RF wireless signals for temporal and spatial focusing in strong multipath channels [39], but is now extended for the first time into the optical regime.

Figures 1(a) and 1(b) show an example of the MMF optical field distortion in both the spatial and temporal domain, respectively. Each mode, which is a solution of Maxwell's equations as discussed in Ref. [40], propagates through the MMF at a different group velocity. Therefore, at any MMF output surface point, the optical field is a sum of multiple individual contributions. Hence, when the input is a narrowband coherent optical source, highly structured interference effects will be observed in the intensity distribution across the end of the MMF surface, resulting in the intensity speckle pattern shown in Fig. 1(a). In this experiment, a 25-m-long step-index MMF (Thorlabs FG200LCC) with a 200 μm core diameter is used. A tunable single-frequency laser in the optical C-band (1530–1565 nm) is focused into the MMF through free-space coupling. The speckle pattern is recorded by an infrared (IR) charge-coupled device (CCD) camera. As discussed in Ref. [14], when a short pulse is transmitted, the spread of time delays associated with various paths is related to the frequency dependence of the speckle pattern (see Visualization 1 for an animation regarding the frequency dependence of the MMF speckle pattern). Moreover, at any specific spatial location, the output fields exhibit random substructures in time, with uncorrelated time responses at different locations. Figure 1(b) shows the time spread at one output location of the MMF sampled by a standard single-mode fiber (SMF, 8 μm core diameter); note that the fiber length of 25 m was chosen for convenience in observing the time spread on a 20-GHz-bandwidth photodetector.

The experimental setup for MMF characterization and pulse compression is shown in Fig. 2. Unlike the speckle pattern measurements in Fig. 1, here we use a 1 m length of the same MMF with a different launch condition to limit the temporal spread to below ~20 ps, which fits within the time aperture of the pulse shaper (Finisar WaveShaper 1000S). A mode-locked fiber laser is used as the input optical field, with its spectrum bandpass filtered to pass 1534–1550 nm (2 THz bandwidth) in order to fit in the quasi-phase matching acceptance bandwidth of the nonlinear waveguide in the following intensity autocorrelator. [The same filtered, mode-locked fiber laser is used as the input for Fig. 1(b)]. The distorted output field is sampled spatially by a SMF, spectral shaped by a pulse shaper, and then measured by an intensity autocorrelator. It is worth mentioning

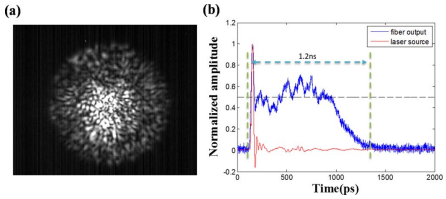

Fig. 1. 25 m multimode fiber (MMF) (a) intensity speckle pattern at fiber output surface with single-frequency input and (b) time spread with broadband ultrafast pulse input. In (b), the red trace is the impulse response of the detection system with a femtosecond pulse input, and the blue trace is the MMF time spread due to modal dispersion.

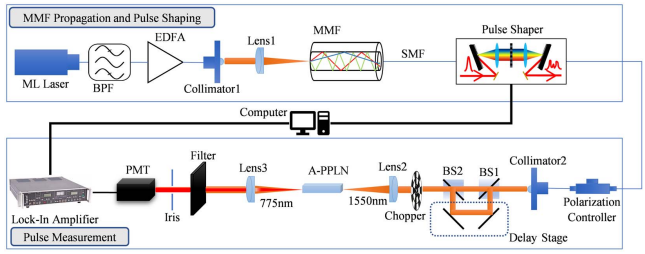

Fig. 2. Experimental setup of optical field characterization and pulse compensation. MMF, multimode fiber; ML Laser, mode-locked laser; BPF, bandpass filter; EDFA, erbium-doped fiber amplifier; SMF, single-mode fiber; BS, beam splitter; A-PPLN, aperiodically poled lithium niobite crystal; PMT, photomultiplier tube.

that the second-harmonic generation (SHG) in the intensity autocorrelator is achieved by using an aperiodically poled lithium niobite (A-PPLN) waveguide, offering significant advantage in the SHG sensitivity [41]. As for the characterization of the MMF impulse response at a specific output location, $H(\omega) = |H(\omega)|e^{j\phi(\omega)}$, a pulse-shaping technique is applied to retrieve the spectral phase $\phi(\omega)$, and to implement spectral phase compensation, i.e., applying $[-\phi(\omega)]$ on the pulse shaper. SHG is used to guide the phase compensation; the spectral phase is adjusted to maximize the SHG yield (either using just one arm of the autocorrelator or setting the autocorrelator delay to zero).

In detail, the spectrum of the output field is equally divided into N sections with $\omega_k = \omega_0 + (k-1)\Delta\omega$ (k is a positive integer), $N = 100$ in this experiment, in order to have fine-enough spectral resolution (20 GHz, 0.16 nm) for resolving the spread in the time domain. The spectral phase is characterized section by section, starting from section 3. (Note that the spectral phase has two degrees of freedom, which define the pulse's group delay and overall phase; the group delay does not affect the pulse shape or the SHG reading and needs not be characterized for our purposes.) For example, the phase value of frequency section k, ϕ_k, is characterized after the phase values of previous $k-1$ sections are already acquired and compensated by programming the pulse shaper, while sections $k+1$ to section N are blocked. In this case, the MMF output field can be written as

$$E_{\mathrm{MMF}} = \sum_{i=1}^{k-1} E_i e^{j\omega_i t} + E_k e^{j\omega_k t}, \tag{1}$$

where $E_i = |E_i|e^{j\phi_i}$. In general, we write the phase at frequency ω_i as $\phi_i = \tilde{\phi}_i + \phi_{i,\mathrm{shaper}}$, where $\tilde{\phi}_i$ is the phase after the fiber and $\phi_{i,\mathrm{shaper}}$ is the phase applied by the pulse shaper. Here we take $\phi_i = 0$ for $i \le k-1$, which corresponds to the assumption that all frequencies $\omega_i < \omega_k$ have already been phase compensated. Assuming broadband phase matching, the time average second-harmonic intensity may be written as

$$\langle I_{\mathrm{SHG}} \rangle = \langle I_{\mathrm{SHG},o} \rangle + \langle I_{\mathrm{SHG}}(\phi_k) \rangle, \tag{2a}$$

where the $\langle I_{\mathrm{SHG},o} \rangle$ term is independent of ϕ_k, and $\langle \ldots \rangle$ represents the time average. We may also write

$$\langle I_{\mathrm{SHG}}(\phi_k)\rangle \sim \left\langle E_k \sum_{a=1}^{k-1}\sum_{b=1}^{k-1}\sum_{c=1}^{k-1} E_a E_b^* E_c^* e^{j(\omega_k+\omega_a-\omega_b-\omega_c)t} + \text{c.c.} \right\rangle. \tag{2b}$$

Information on ϕ_k is contained in the $\langle I_{\mathrm{SHG}}(\phi_k)\rangle$ term. Note that the time average in Eq. (2b) picks out frequency combinations for which $\omega_k + \omega_a - \omega_b - \omega_c = 0$. Since $\phi_i = 0$ for $i \le k-1$, we have

$$\langle I_{\mathrm{SHG}}\rangle(\phi_k) \sim \cos(\phi_k)|E_k| \sum_{a=1}^{k-1}\sum_{b=1}^{k-1}\sum_{c=1,\, k+a=b+c}^{k-1} |E_a E_b E_c|. \tag{3}$$

Thus, the acquired SHG intensity read by the lock-in amplifier shows a simple sinusoidal dependence with respect to the phase value applied by the pulse shaper. In this experiment, eight equally spaced phase values, between 0 and 2π, are applied on each frequency section. This results in eight corresponding SHG intensity values which oversample the $\cos(\phi_k)$ function. Therefore, by performing a fast Fourier transform of the SHG data, $\tilde{\phi}_k$ can be retrieved with a resolution limited only to the experimental signal-to-noise. Then the negative value of the phase retrieved is applied by the pulse shaper, ensuring that $\tilde{\phi}_k + \phi_{k,\mathrm{shaper}} = 0$. This finishes the kth section, and we repeat this procedure for the remaining sections.

Figure 3 shows normalized intensity autocorrelation measurements of the output of the 1 m MMF, both with and without spectral phase compensation. The data are in close agreement with simulated results calculated from the measured power spectrum and retrieved phase information. Here the background is subtracted for display reasons. The autocorrelation in Fig. 3(a) has a broad envelope with a narrow spike in the middle, with a roughly 2:1 peak-to-envelope contrast in the background-free case (3:2:1 peak-to-envelope-to-background contrast with the background retained). This is the signature of a finite duration noise burst [42], as expected for a temporal speckle field caused by modal dispersion broadening. The 15 ps width of the broad envelope suggests a total broadening of ~10 ps. After spectral phase compensation, the output field is compressed back to the transform limit, Fig. 3(b), with a 2:0 autocorrelation contrast ratio in the background-free case (3:1 before subtracting the background), and ~670 fs full width at half-maximum (FWHM) autocorrelation width. The peak SHG signal after pulse compression is increased by about an order of magnitude compared to the SHG signal of the noise-like output field.

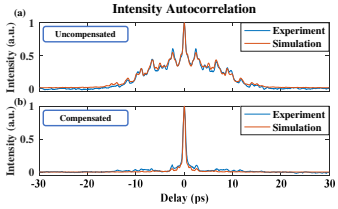

Fig. 3. Experimental and simulation results for MMF output optical field characterization and pulse compensation. (a) Intensity autocorrelation trace of MMF output field (MMF impulse response) in experiment (blue) and in simulation (red). (b) Intensity autocorrelation of compensated pulse in experiment (blue) and in simulation (red).

In a MMF with strong modal dispersion effects, the temporal and frequency speckles are expected to decorrelate rapidly in the spatial coordinate. We tested this expectation by using a standard SMF mounted on a translation stage to sample the field at two locations on the output surface of the MMF separated by 10 μm. The MMF channel responses at the two output spots are plotted in Fig. 4 in both frequency and time domains. The autocorrelation data in Fig. 3 corresponds to output 1 in Fig. 4. The output field at any specific spatial spot acquires random substructures in both time (temporal speckle) and frequency (spectral speckle). The temporal and spectral profiles are of course related by the Fourier transform. Comparison of the temporal and spectral profiles at the two output locations show a similar character but quite distinct details, confirming the expected decorrelation. The channel impulse responses shown in Figs. 4(c) and 4(d) are calculated from the power spectra measured by an optical spectrum analyzer (OSA) and the phase responses characterized via pulse shaping. As can be seen, multiple copies of transmitted pulses are received, with random attenuation (amplitude), delays, and phases. A time delay spread of ~10 ps can be observed at both output locations, but with different substructures. These data resolve the temporal speckles, which are averaged out in the photodetector measurements of Fig. 1(b). The multiple deep fades in the power spectra of Figs. 4(a) and 4(b) are a manifestation of the speckle in frequency and are in analogy with the deep fades that occur in strongly multipath RF channels [1].

The decorrelation of the MMF channels at different output locations is further proven by focusing a transform-limited ultrafast pulse in space and time. As seen in Figs. 5(a)–5(d), when the pulse shaper is programmed to compensate the channel response corresponding to output 1, a strong peak will appear on the intensity autocorrelation trace measured at output 1, whereas the intensity autocorrelation measured at output 2 indicates a noise-like field. Conversely, when the pulse shaper is configured to compensate the channel corresponding to output 2, the field at output 1 remains noise-like, with compression observed at output 2. Note that the peak values of the solid traces in Figs. 5(b) and 5(c) are normalized to the peak values

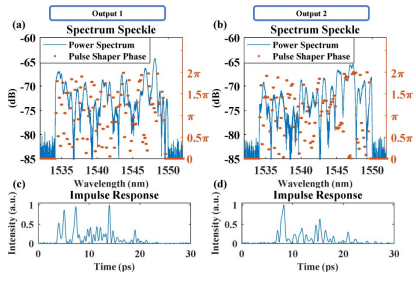

Fig. 4. Spectral speckles and temporal speckles at two different output locations. (a), (b) Spectral speckles at output location 1 and at output location 2. Power spectra (blue solid) are measured using optical spectrum analyzer (OSA), and phases (red dot) programmed on the pulse shaper are used to compensate the output fields. (c), (d) Temporal speckles at output location 1 and at output location 2. The impulse responses are calculated from the frequency responses shown in (a) and (b) by inverse Fourier transform.

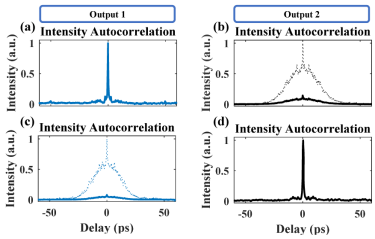

Fig. 5. Spatial and temporal focusing at MMF output surface using spectral phase compensation. (a), (b) The optical field at output 1 is compensated. The field at output 1 is a transform-limited pulse whereas the field at output 2 remains noise-like. The solid trace in (b) is normalized to the peak value in (a). (c), (d) The optical field at output 2 is compensated. The field at output 2 is a transform-limited pulse whereas the field at output 1 remains noise-like. The solid trace in (c) is normalized to the peak value in (d). The dotted lines in (b) and (c) are zoomed vertically.

of the traces in Figs. 5(a) and 5(d), respectively. The dotted traces in Figs. 5(b) and 5(c) are zoomed-in in the vertical scale to better display the 2:1 peak-to-envelope contrast of the noise-like fields. The spatially selective peaking in a specific input–output channel demonstrates space–time focusing of the MMF system. In this case, the transmitted information can be encoded for compression at a specific output spot, while the peak intensity remains low and potentially more difficult to detect at other output locations. This capability may bring opportunities for covert sharing of a MMF for multiple communication channels.

To summarize, we have demonstrated space–time focusing of broadband ultrafast pulses distorted by modal dispersion in a MMF. Our approach uses phase compensation in the spectral domain (pulse shaping) and does not require interference with a reference field. Furthermore, although the current report employs a commercial pulse shaper constructed from discrete components, pulse shapers can also be realized on chip [43–45], opening possibilities for highly compact shaper-MMF modules. In contrast, wavefront-shaping techniques rely on spatial light modulators, which are inherently free-space components. This work could contribute to new opportunities for nonlinear microscopy and imaging or space-division multiplexed optical communications through MMF.

Acknowledgment. The authors thank former group member Dr. Joseph Lukens for designing the A-PPLN waveguide and Dr. Carsten Langrock and Dr. Martin M. Feijer for fabrication of the A-PPLN waveguide. The authors also thank senior scientist Dr. Daniel Leaird and former group members Dr. Ogaga Odele and Dr. Yihan Li for technical help.

REFERENCES

1. M.-G. Di Benedetto, *UWB Communication Systems: A Comprehensive Overview* (Hindawi, 2006).
2. A. F. Molisch, *Wireless Communications* (Wiley, 2012).
3. A. Dezfooliyan and A. M. Weiner, Opt. Lett. **38**, 4946 (2013).
4. D. R. Dowling, J. Acoust. Soc. Am. **95**, 1450 (1994).
5. A. Derode, P. Roux, and M. Fink, Phys. Rev. Lett. **75**, 4206 (1995).
6. K. B. Smith, A. A. Abrantes, and A. Larraza, J. Acoust. Soc. Am. **113**, 3095 (2003).
7. J. W. Goodman, *Speckle Phenomena in Optics: Theory and Applications* (Roberts and Company, 2007).
8. I. M. Vellekoop and A. Mosk, Opt. Lett. **32**, 2309 (2007).
9. R. Tyson, *Principles of Adaptive Optics* (CRC Press, 2010).
10. S. Popoff, G. Lerosey, M. Fink, A. C. Boccara, and S. Gigan, Nat. Commun. **1**, 81 (2010).
11. S. Popoff, G. Lerosey, R. Carminati, M. Fink, A. Boccara, and S. Gigan, Phys. Rev. Lett. **104**, 100601 (2010).
12. X. Xu, H. Liu, and L. V. Wang, Nat. Photonics **5**, 154 (2011).
13. A. P. Mosk, A. Lagendijk, G. Lerosey, and M. Fink, Nat. Photonics **6**, 283 (2012).
14. A. M. Weiner, Nat. Photonics **5**, 332 (2011).
15. M. Webster, K. Webb, and A. Weiner, Phys. Rev. Lett. **88**, 033901 (2002).
16. J. Bertolotti, E. G. van Putten, C. Blum, A. Lagendijk, W. L. Vos, and A. P. Mosk, Nature **491**, 232 (2012).
17. O. Katz, E. Small, Y. Bromberg, and Y. Silberberg, Nat. Photonics **5**, 372 (2011).
18. J. Aulbach, B. Gjonaj, P. M. Johnson, A. P. Mosk, and A. Lagendijk, Phys. Rev. Lett. **106**, 103901 (2011).
19. D. J. McCabe, A. Tajalli, D. R. Austin, P. Bondareff, I. A. Walmsley, S. Gigan, and B. Chatel, Nat. Commun. **2**, 447 (2011).
20. M. Mounaix, D. Andreoli, H. Defienne, G. Volpe, O. Katz, S. Grésillon, and S. Gigan, Phys. Rev. Lett. **116**, 253901 (2016).
21. Y. Choi, C. Yoon, M. Kim, T. D. Yang, C. Fang-Yen, R. R. Dasari, K. J. Lee, and W. Choi, Phys. Rev. Lett. **109**, 203901 (2012).
22. M. N'Gom, T. B. Norris, E. Michielssen, and R. R. Nadakuditi, Opt. Lett. **43**, 419 (2018).
23. D. Richardson, J. Fini, and L. Nelson, Nat. Photonics **7**, 354 (2013).
24. T. Mori, T. Sakamoto, M. Wada, T. Yamamoto, and F. Yamamoto, J. Lightwave Technol. **32**, 2468 (2014).
25. H. Defienne, M. Barbieri, I. A. Walmsley, B. J. Smith, and S. Gigan, Sci. Adv. **2**, e1501054 (2016).
26. L. G. Wright, Z. Liu, D. A. Nolan, M.-J. Li, D. N. Christodoulides, and F. W. Wise, Nat. Photonics **10**, 771 (2016).
27. K. Krupa, A. Tonello, B. M. Shalaby, M. Fabert, A. Barthélémy, G. Millot, S. Wabnitz, and V. Couderc, Nat. Photonics **11**, 237 (2017).
28. R. Di Leonardo and S. Bianchi, Opt. Express **19**, 247 (2011).
29. I. N. Papadopoulos, S. Farahi, C. Moser, and D. Psaltis, Opt. Express **20**, 10583 (2012).
30. B. Redding, S. M. Popoff, and H. Cao, Opt. Express **21**, 6584 (2013).
31. N. Coluccelli, M. Cassinerio, B. Redding, H. Cao, P. Laporta, and G. Galzerano, Nat. Commun. **7**, 12995 (2016).
32. R. Rokitski and S. Fainman, Opt. Express **11**, 1497 (2003).
33. Z. Guang, M. Rhodes, and R. Trebino, Appl. Opt. **56**, 3319 (2017).
34. E. E. Morales-Delgado, S. Farahi, I. N. Papadopoulos, D. Psaltis, and C. Moser, Opt. Express **23**, 9109 (2015).
35. E. E. Morales-Delgado, D. Psaltis, and C. Moser, Opt. Express **23**, 32158 (2015).
36. B. Liu and A. M. Weiner, in *Conference on Lasers and Electro-Optics* (Optical Society of America, 2018), paper SF3N-2.
37. A. M. Weiner, Rev. Sci. Instrum. **71**, 1929 (2000).
38. A. M. Weiner, Opt. Commun. **284**, 3669 (2011).
39. A. Dezfooliyan and A. M. Weiner, IET Commun. **7**, 1287 (2013).
40. J. Gowar, *Optical Communication Systems* (Prentice-Hall, 1984).
41. S.-D. Yang, A. M. Weiner, K. R. Parameswaran, and M. M. Fejer, Opt. Lett. **29**, 2070 (2004).
42. A. Weiner, *Ultrafast Optics* (Wiley, 2009).
43. N. K. Fontaine, R. P. Scott, C. Yang, D. J. Geisler, J. P. Heritage, K. Okamoto, and S. Yoo, Opt. Lett. **33**, 1714 (2008).
44. S. Tahvili, S. Latkowski, B. Smalbrugge, X. J. M. Leijtens, P. J. Williams, M. J. Wale, J. Parra-Cetina, R. Maldonado-Basilio, P. Landais, and M. K. Smit, IEEE Photon. Technol. Lett. **25**, 450 (2013).
45. A. J. Metcalf, H.-J. Kim, D. E. Leaird, J. A. Jaramillo-Villegas, K. A. McKinzie, V. Lal, A. Hosseini, G. E. Hoefler, F. Kish, and A. M. Weiner, Opt. Express **24**, 23925 (2016).